

---

---

This manuscript is a preprint and will be shortly submitted for publication to a scientific journal. As a function of the peer-reviewing process that this manuscript will undergo, its structure and content may change.

If accepted, the final version of this manuscript will be available via the 'Peer-reviewed Publication DOI' link on the right-hand side of this webpage. Please feel free to contact any of the authors; we welcome feedback.

---

---

# From space-time landslide susceptibility to landslide risk forecast

Tengfei Wang<sup>1,2</sup>, Ashok Dahal<sup>2</sup>, Zhice Fang<sup>2,3</sup>, Cees van Westen<sup>2</sup>, Kunlong Yin<sup>1\*</sup>, Luigi Lombardo<sup>2</sup>

<sup>1</sup> Faculty of Engineering, China University of Geosciences, Wuhan, 430074, China;

<sup>2</sup> Faculty of Geo-Information Science and Earth Observation (ITC), University of Twente, Enschede, AE 7500, Netherlands;

<sup>3</sup> Institute of Geophysics and Geomatics, China University of Geosciences, Wuhan, 430074, China;

\* Corresponding author: Kunlong Yin ([yinkl@cug.edu.cn](mailto:yinkl@cug.edu.cn))

**Abstract:** The literature on landslide susceptibility is rich with examples that span a large number of topics. However, the component that pertains to the extension of the susceptibility framework toward space-time modeling is largely unexplored. This statement is even more valid when looking at the landslide risk context, where hardly any scientific contribution investigates risk dynamics in space and time. This manuscript proposes a modeling protocol where a dynamic landslide susceptibility is obtained via a binomial Generalized Additive Model whose inventories span nine years (from 2013 to 2021). To perform the analyses, the data cube is organized with a mapping unit made of slope units (26,333) repeated over an annual temporal unit (for a total of 236,997). This phase already features a number of interesting modeling experiments that have hardly appeared in the landslide literature (e.g., variable interaction plots). However, the main innovative effort is in the subsequent phase of the protocol we propose, for we used climate projections of the main trigger (rainfall) to obtain future estimates of yearly susceptibility patterns. These are also combined with the projection of urban settlements and associated populations to obtain a dynamic risk model (under the assumption that vulnerability = 1). Overall, this is a unique example of such a modeling routine and a potential standard to be followed for administrations to make informed decisions on future urban development.

**Keywords:** Space-time statistics; Dynamic landslide susceptibility; Landslide risk; Future projections

## 1 Introduction

Historical advancements in landslide susceptibility modeling (through data-driven solutions) explored a number of themes, spanning from the most suitable mapping unit on to base the analyses (e.g., [Van Den Eeckhaut et al., 2009](#); [Schlögel et al., 2018](#)), to the most suitable predictor set (e.g., [Budimir et al., 2015](#); [Ozturk et al., 2021](#)), passing from experiments on the most appropriate sampling strategies ([Yilmaz, 2010](#); [Conoscenti et al., 2016](#)) to take and encompassing solutions to remove potential biases due to incomplete inventories ([Stegeret al., 2016](#); [Lima et al., 2021](#)).

As for the most recent trends in landslide susceptibility modeling, most contributions focused on the

33 choice of modeling architectures able to ensure the highest predictive performance ([Reichenbach et al., 2018](#);  
34 [Lima et al., 2022](#)). In this overall scenario, very isolated efforts have been put forward to move toward  
35 space-time solutions ([Samia et al., 2017](#); [Lombardo et al., 2020](#)). These are models whose structure allows  
36 for modeling the distribution of landslide presence/absence instances simultaneously across the geographic  
37 space and across time. The way they usually work is to incorporate explanatory variables whose  
38 spatiotemporal variation reflects changes in the distribution of multi-temporal landslide occurrences. This  
39 can be done explicitly (e.g., using rainfall or vegetation parameters; [Wang et al., 2022a](#); [Mondini et al.,](#)  
40 [2023](#)) or at the latent level ([Lombardo et al., 2018, 2019](#)). Some exceptions to this rule do exist and they  
41 represent very innovative examples where the typical structure of space-time data-driven solutions is used to  
42 mimic landslide early warning systems (e.g., [Steger et al., 2022](#); [Nocentini et al., 2023](#)).

43 However, even if recent studies are pointing towards an increasing interest in dynamic landslide  
44 predictions, these are mostly confined to the occurrence probability case ([Segoni et al., 2018](#); [Lombardo](#)  
45 [and Tanyas, 2020](#)). In other words, the number of contributions beyond the susceptibility context, even  
46 including space-time cases, is a minority ([Tyagi et al., 2022](#)). This is an issue that certainly exists for  
47 landslide hazard assessment contributions (see, [Van Westen et al., 2006](#)), and becomes even more evident  
48 in the case of landslide risk research (see, [Corominas et al., 2014](#)). Focusing on risk aspects, what stands  
49 out is that most of the contributions on landslide risk are site-specific ([Dai et al., 2002](#); [Glade et al., 2005](#))  
50 and mainly involve pure spatial assessments ([Lateltin et al., 2005](#); [Abella and Van Westen, 2007](#)). Conversely,  
51 hardly any examples can be found where the landslide risk assumes space-time connotations ([Remondo et](#)  
52 [al., 2008](#); [Rossi et al., 2019](#)).

53 The main reasons behind such discrepancies are the requirement of such type of assessment. For  
54 instance, risk assessment requires data on the distribution of exposure ([Pellicani et al., 2014](#); [Emberson et al.,](#)  
55 [2020](#)) and vulnerability ([Galli and Guzzetti, 2007](#); [Kaynia et al., 2008](#)). The former can still be found to some  
56 extent, with products that report building, infrastructure, and population density distributions. However,  
57 vulnerability information ([Ahmed, 2021](#); [Peduto et al., 2017](#)) and specifically on vulnerability curves  
58 estimated for specific infrastructures ([Quan Luna et al., 2011](#); [Uzielli et al., 2015](#)) are hardly available,  
59 especially when the scale of the analyses involves large spatiotemporal domains ([Pascale et al., 2010](#); [Luo et](#)  
60 [al., 2023](#)). And yet, this constitutes the most relevant information for decision-makers because it is precisely  
61 the combination of exposure and vulnerability that controls the potential losses due to a given landslide  
62 occurrence ([Petley, 2012](#); [Papathoma-Köhle et al., 2015](#)).

63 In this context, we devised our research question and the experimental design presented in this  
64 contribution. Specifically, due to the prohibitive task behind the acquisition of vulnerability data over

65 large regions and over time, we hypothesize that if a landslide occurs, it would damage irreparably any  
66 structure in its path. This is certainly a strong assumption but it would allow to produce landslide risk  
67 estimates if building and population data are combined with a susceptibility map. To this idea, we add a  
68 further dimension by framing the proposed routine in a space-time modeling context. We do so thanks to  
69 a rich landslide database collected over a decade in the northeastern sector of Chongqing, China. There,  
70 a systematic landslide mapping protocol has been set up over the years due to historical disastrous  
71 events (e.g., [Zhao et al., 2018](#)), equipping local authorities and academic institutions with complete multi-  
72 temporal inventories. Due to analogous reasons, the area is also equipped with a dense rain gauge network  
73 ([Chen et al., 2019](#)), making it an ideal case for testing space-time modeling techniques. There, we will  
74 calibrate and validate a space-time susceptibility model with the intent of using it as a base for future  
75 simulations, which we will then combine with urban and population projections to obtain future  
76 landslide risk scenarios.

## 77 **2 Study area**

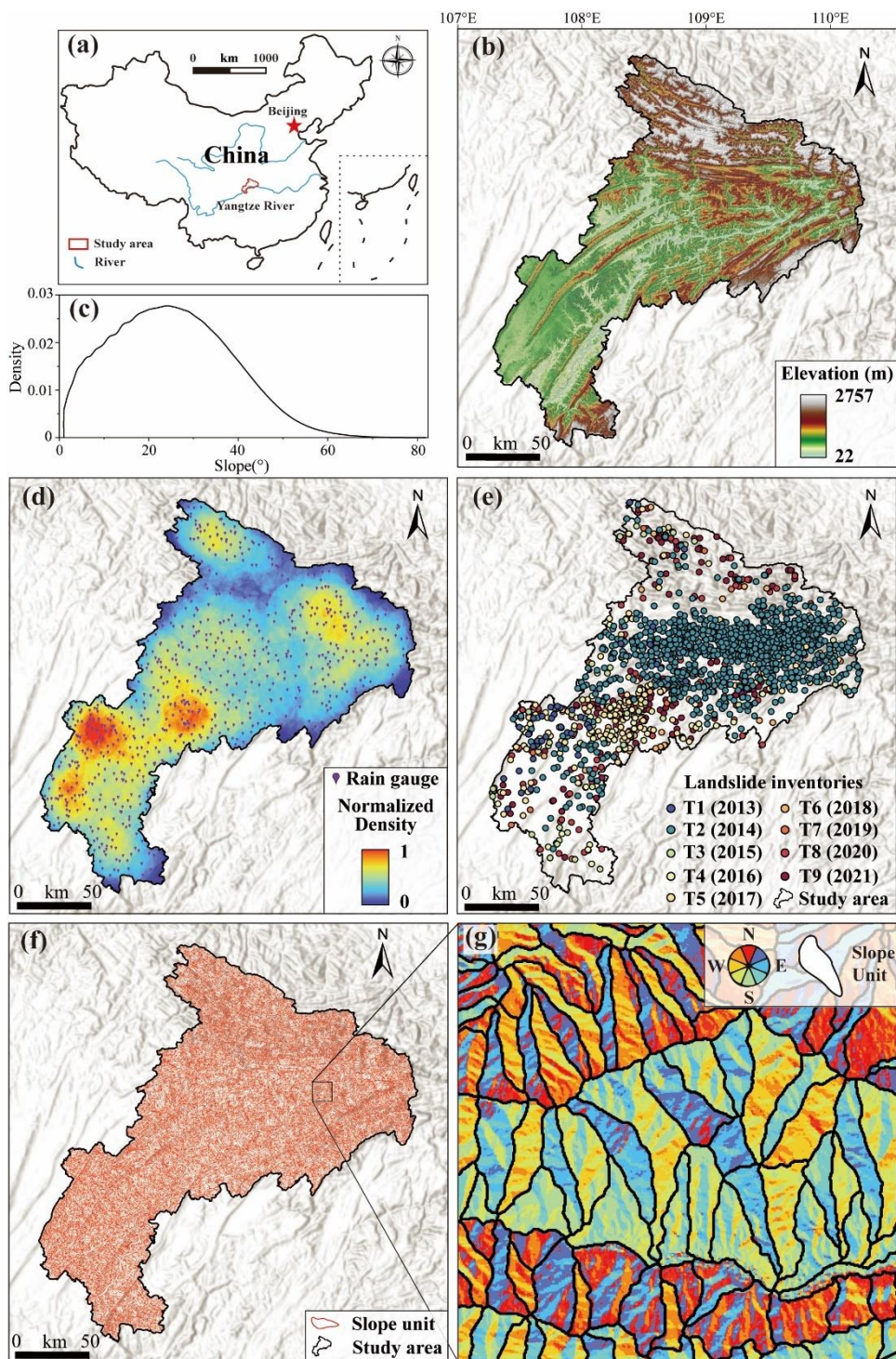
### 78 **2.1 Geography and geological condition**

79 The study site is located in the southeast of Chongqing, China, and extends over an area of  $\sim 34,000$   
80  $\text{km}^2$  (see Fig. 1a). It is located on the northeastern edge of the Sichuan Basin, and as a result of an  
81 ongoing tectonic compression started in the late Mesozoic, the topography features numerous folds and  
82 high peaks, low hills, and incised valleys. The mountain ranges are oriented either NE–SW or E–W, with  
83 mountain elevations between 800–2700 m, while valleys occupy a much lower position in the topographic  
84 profile, with elevations ranging from 300–1000 m (see Fig. 1b). Due to the complex nature of the terrain,  
85 slopes cover a wide range of 0–60°, mostly centered at 25° (see Fig. 1c). The geomorphology is structurally  
86 controlled, featuring anticlinal mountains and synclinal valleys, with trends being roughly consistent  
87 with the directions of tectonic lineaments. The Yangtze River, the longest river in Asia, flows from  
88 west to east in the study area.

### 89 **2.2 Rainfall condition**

90 The region is exposed to a subtropical monsoon climate, with four distinct seasons and high  
91 precipitation discharges. Thousands of rain gauges have been installed in the last decade to monitor the  
92 rainy weather and characterize the monsoon-influenced humid subtropical climate. These are all new-  
93 generation weather stations, automatically recording and airing the digital transcripts to the data center  
94 daily. The very same data was shared from the meteorological agency of Chongqing to support this  
95 research, covering the period from January 1<sup>st</sup> 2013 to December 31<sup>st</sup> 2021, and corresponding to the

96 precipitation signal captured across 729 rain gauges (see Fig. 1d).



97  
98 Figure 1: Panel (a) locates the study site concerning the Chinese territory; Panel (b) presents an overview of the  
99 terrain; Panel (c) graphically shows the summary statistics of the slope steepness; Panel (d) geographically plots  
100 the distribution density of the rain gauges; Panel (e) represents the multi-temporal landslide inventories; Panels  
101 (f) and (g) show the slope unit partition and a dedicated zoom, respectively.

### 102 2.3 Landslide inventory

103 Chongqing widely hosts landslide-prone steep terrains, especially in the northeast sector, where  
104 landslides tend to concentrate along the Yangtze River and some of its tributaries, especially in the regions  
105 of Wanzhou, Yunyang, and Wushan. The genesis of the failure mechanism in the area has been documented  
106 in several scientific contributions, highlighting the primary role of seasonal, intense, and prolonged rainfall  
107 events (see, [Zhang et al., 2023](#)), followed by the fluctuation of reservoir water level and anthropic  
108 interventions involving slope cuts. From 2013 to 2021, the number of landslides with detailed records  
109 (location and date) in the study area reached a total number of 2978, out of which, 2142 landslides occurred  
110 just in 2014 (see Fig. 1e). These account for 72 % of the total failures over the 9 examined years, and  
111 were triggered by an extreme storm ([Li et al., 2022](#)). The vast majority of landslides manifest as shallow  
112 translational slides. As for the materials the failures mostly involve, these correspond to sandstone, mudstone,  
113 and intercalations of the latter into the first ([Wang et al., 2019](#)).

## 114 **3 Material and methods**

### 115 **3.1 Mapping and temporal units**

116 To predict the occurrence of landslides in an area, it is necessary to first select a suitable mapping  
117 unit. Among the units explored in previous studies, four main types can be found: geomorphological units  
118 ([Meijerink, 1988](#); [Seijmonsbergen et al., 2013](#)), unique condition units ([Calcaterra et al., 2010](#); [Titti et al.,](#)  
119 [2021](#)), slope units ([Carrara et al., 1991](#)), and grid-cells ([Fang et al., 2020](#); [Lima et al., 2021](#)). Slope  
120 units have recently gained more and more attention, as they represent the morpho-dynamic response of  
121 slopes in which the landslides initiated. As a result, specifically for data-driven models, they offer a partition  
122 for which any landslide activation should be mostly independent (or very weakly dependent) from a potential  
123 failure occurring in an adjacent slope. For this reason, the “slope unit” (SU) is selected here to be the  
124 designated mapping unit in this study ([Alvioli et al., 2016](#)). In short, SU can be mapped between drainage  
125 and divide lines. Their calculation relies on the same foundation behind catchment delineation ([Jenson and](#)  
126 [Domingue, 1988](#)) because they theoretically correspond to half-basins ([Carrara, 1988](#)). Notably, the study  
127 area includes both rough terrain and near-flat areas in the form of plains, tablelands, and water bodies.  
128 The latter usually correspond to trivial areas where no landslide can physically take place. The latest  
129 version of the software *r.slopeunits* by ([Alvioli et al., 2016](#)) allows one to remove flat areas from the SU  
130 generation, excluding them based on the results pass by the *r.geomorphon* module ([Jasiewicz and Stepinski,](#)  
131 [2013](#)). After a number of sensitivity (unreported) tests, the final number of SU was 26,333, ranging in  
132 size from  $2.04 \cdot 10^4 \text{ m}^2$  to  $1.5 \cdot 10^7 \text{ m}^2$  ( $\mu = 1.25 \cdot 10^6 \text{ m}^2$ ,  $\sigma = 1.23 \cdot 10^6 \text{ m}^2$ ). This corresponds to an average  
133 density of one SU approximately every  $1.3 \text{ km}^2$  (see Fig. 1f and 1g).

134 As for how we partitioned the temporal dimension, we opted for a yearly unit (YU). Therefore, the  
135 landslide inventory was divided into nine consecutive YUs. The combination of the spatial and temporal  
136 dimensions eventually led to a total of 236,997 SUs (26,333 SUs multiplied by 9 YUs).

### 137 **3.2 Covariates**

138 The covariates set includes environmental characteristics related to geology, geomorphology, and  
139 meteorology to cover different aspects related to the genesis of landslides. Some of them featured properties  
140 that remain essentially constant within the time scale of the analyses. For instance, lithological classes can  
141 be considered time-invariant. Analogously, terrain characteristics also exhibit a slow rate of temporal  
142 variation and can also be approximated to be time-invariant (or at least there is no topographic data  
143 acquired frequently enough to support a different solution). Conversely, vegetation density and rainfall  
144 patterns do change at a fast rate, allowing for a space-time model to incorporate their dynamic signal.

145 Table 1 lists the initial covariate set we considered for this study. It includes 14 static covariates and  
146 3 dynamic ones. Out of the static group, ten are derivatives of a 30 m·30 m resolution digital elevation  
147 model (DEM). We recall here that a SU partitions the landscapes into high-order half-basins with an  
148 average areal extent of  $1.25 \cdot 10^6 m^2$ . Therefore, their surface expression can host hundreds or even  
149 thousands of 30 m·30 m grid cells. For this reason, we summarized the corresponding grid-based covariates'  
150 distribution in a SU, through their respective mean and standard deviation values. We also computed a  
151 static covariate capable of expressing the structural geology typical of each SU. We did this by  
152 combining terrain characteristics with local measurements of strata direction and dip angles. To do so,  
153 we followed the same approach shown by [Luo et al. \(2021\)](#). We then categorized the resulting map  
154 categorized the results into 3 structural classes (dip slope, anti-dip slope, and cross-dip slope) and assigned  
155 the predominant type to each SU. The predominant type criterion was also used to aggregate the soil type  
156 (see, [Li et al., 2009](#)) and land use (see, [Gong et al., 2020](#)) 1:250,000 scale information per SU.

157 We also aggregated on a SU basis the yearly sum and daily maximum rainfall interpolated from the local  
158 rain gauge network. To perform the interpolation, we opted for an Ordinary Kriging ([Cressie, 1988](#)). As  
159 for the aggregation method, we assigned the mean rainfall value per SU.

160 The normalized difference vegetation index (NDVI) was also featured in the covariate set by computing  
161 the mean value of all annual mean values across pixels falling in a given SU.

162  
163  
164  
165

Table 1: Summary of initial covariates used in this study

Type	Covariates	Description	Source
Static	$Slope_{\mu}$	Terrain slope mean	30·30m DEM
	$Slope_{\sigma}$	Terrain slope St. dev.	
	$PLCR_{\mu}$	Planar curvature mean	
	$PLCR_{\sigma}$	Planar curvature St. dev.	
	$PRCR_{\mu}$	Profile curvature mean	
	$PRCR_{\sigma}$	Profile curvature St. dev.	
	$Northness_{\mu}$	Northness mean	
	$Northness_{\sigma}$	Northness St.dev.	
	$Eastness_{\mu}$	Eastness mean	
	$Eastness_{\sigma}$	Eastness St.dev.	
	$SLST$	Majority class of slope structure in each slope unit	Terrain Slope and tendency, Rock formations tendency, and dip
	$Lithology$		Lithological map, 1:250,000
	$Soil\ Type$	Majority class in each slope unit	Soil type map, 1:250,000
	$Land\ use\ type$		Land use type, 1:250,000
Dynamic	$Daily\ maximum\ rainfall$	Maximum daily rainfall per year in each slope unit	National rain gauge
	$Annual\ sum\ rainfall$	Sum rainfall per year in each slope unit	
	$NDVI_{\mu}$	Mean NDVI value per year in each slope unit	Landsat 7 images from Google engine

### 167 3.3 Rainfall projections

168 As part of the modeling protocol, we present in this manuscript, we will train a space-time  
169 susceptibility model, from which we will simulate future landslide occurrence probabilities  
170 corresponding to various rainfall projections. Therefore, it was necessary to introduce a pre-processing  
171 step to obtain rainfall scenarios. The pre-processing method approach first calculates the annual average,  
172 maxima, and standard deviation from the projected climate change scenarios from Coupled Model  
173 Intercomparison Project CMIP-5 models (Taylor et al., 2012), which has been bias-corrected by using the  
174 method developed by Thrasher et al. (2012) and distributed under the NASA Earth Exchange Global Daily  
175 Downscaled Projections NEX-GDDP program of National Aeronautics and Space Administration  
176 (NASA). From these bias-corrected products, we selected the Representative Concentration Pathways  
177 (RCP) -4.5 scenario, which represents the climate projections showing the level of radiative forcing by  
178 greenhouse gas emissions stabilizing at  $4.5\ W/m^2$  by 2100. This is because the projection of landslide  
179 hazard is estimated for the next eight years, and climate extremes due to much harsher scenarios (such as  
180 RCP-8.5) which are expected by the end of the century, are still not fully surfaced. With the selected  
181 scenario and different models, we ensembled the precipitation scenarios by averaging the annual maximum  
182 and mean projections obtained from different models. The standard deviation, however, is used as a quality  
183 check to ensure there are very unlikely precipitation scenarios that can unnecessarily elevate the



184 susceptibility. With the annual ensembled mean, we then computed the expected annual total  
185 precipitation by multiplying the ensembled mean by 365. This is because the daily climate projection  
186 products are not very reliable and full of uncertainties; therefore, their direct summation may increase  
187 bias. Nevertheless, their annual average forecast is much more reliable and likely to occur; thus, calculating  
188 total annual precipitation by multiplying the annual mean by 365 provided a rough estimate of  
189 precipitation with higher certainty than the summation of daily products. This approach is repeated from  
190 2022-2030 for each year to calculate the rainfall projections for the next eight years.

### 191 **3.4 Generalized additive model**

192 Generalized Additive Models (GAMs) are a class of statistical models capable of estimating the  
193 functional relation existing between dependent and independent variables accommodating for both  
194 linear and nonlinear cases (Hastie and Tibshirani, 1987). In short, this allows for estimating single  
195 regression coefficients for covariates that are linearly linked to the response, and an array of regression  
196 coefficients for covariates that are modeled nonlinearly. The latter is mostly achieved by using splines,  
197 whose nature depends on the nonlinear dependence the user is interested to model (Hastie, 2017).

198 GAMs are suitable to model a number of statistical distributions, welcoming exponential families  
199 such as binomial, Poisson, Gamma, and more. In the context of landslide susceptibility studies, the response  
200 variable expresses two conditions, reflecting whether a given slope may be stable or unstable (Brenning,  
201 2008). For this reason, we opted for a binomial GAM, whose generic structure can be denoted as follows:

$$202 \quad \eta(\pi) = \log\left(\frac{\pi}{1-\pi}\right) = \beta_0 + \sum_{n=0}^{\# \text{ lin. cov.}} \beta_n X_n + \sum_{i=0}^{\# \text{ nonlin. cov.}} f_i x_i \quad (1)$$

203 where  $\eta$  is the logit function,  $\pi$  is the probability of at least a landslide to occur in a given Slope Unit,  
204  $\beta_0$  is the global intercept,  $\beta_n$  are the regression coefficients linearly estimated for each of the covariates  $X_n$   
205 in the model, and  $f_i$  is spline regression functions estimated for each of the covariates  $x_i$  in the model.

206 Notably, a strict definition of a spatial statistical model requires it to treat observations distributed across  
207 the geographic space differently. For instance, interpolators treat measurements as a function of reciprocal  
208 distances (Babak and Deutsch, 2009). But, in most landslide susceptibility examples this is usually not the  
209 case, as the probability assigned to any given mapping unit varies in space purely as a function of covariate  
210 values. In other words, mapping units that are located close to each other are usually treated in the same way  
211 as those that are located far away. Analogous considerations can be made in relation to the temporal  
212 dimension. A strict definition of a temporal statistical model requires it to treat instances distributed across  
213 time differently. For instance, in time-series analysis, model estimates computed for a specific moment also  
214 depend on the signal recorded before, and the strength of such dependence usually decays with time (Beck

215 [et al., 1998](#)). In other words, temporal observations that are close in time are treated differently as compared  
216 to observations that are recorded much earlier. We recall now that the stable/unstable labels in this work are  
217 assigned to SU on an annual basis.

218 Therefore, in addition to terrain, geological and meteorological covariates, we also included a spatial and  
219 a temporal effect to induce proximity dependence in the two respective dimensions. In turn, this defines our  
220 model as a space-time Binomial GAM, which we implemented by using the “mgcv” package ([Wood, S. and](#)  
221 [Wood, M.S., 2015](#)) in “R” ([Ihaka and Gentleman, 1996](#)).

### 222 **3.5 Model validation**

223 Our GAM model serves both explanatory and predictive purposes. The explanatory component  
224 involves interpreting the functional relations estimated for each selected covariate from a geomorphological  
225 perspective. For instance, if a model would return a negative influence of the slope steepness over the  
226 susceptibility, this would not reflect the physical understanding of the failure mechanism. This is one of  
227 the main strengths of statistical models because they can be assessed both on the basis of their scientific  
228 reasonability as well as the performance they produce. Here, we achieve these two elements by fitting a  
229 model that uses 100% of the available spatiotemporal information. As for the performance assessment, we  
230 recall here that the input of a susceptibility model consists of a vector of stable/unstable labels,  
231 conventionally represented by zeroes and ones. However, the output of the model is not discrete but  
232 expressed instead as a continuous range of probabilities. Consequently, when evaluating the performance  
233 of any binary classifier, the requirement is always to convert a posteriori probability spectrum into a  
234 sequence of zeroes and ones. These can then be matched against the original presence/absence  
235 observations, obtaining what is commonly referred to as a confusion matrix. This is made of four  
236 elements namely, True positives (TP), True negatives (TN), False Positives (FP), and False Negatives  
237 (FN). From these, a number of performance derivatives can be obtained, both cut-off dependent and cut-  
238 off independent. In this work, we assessed the performance by measuring  $TP / (FN + TP)$  and  $TN / (TN +$   
239  $FP)$ . These fall in the cutoff-dependent category because a different probability threshold from the one  
240 we set here at the Youden Index ([Fluss et al., 2005](#)), would lead to different accuracy values. Another  
241 performance parameter we consider is the error rate, which corresponds to the average of the  
242 misclassified cases (both FP and FN), normalized with respect to the total samples.

243 To estimate cutoff-independent performance, we opted for the ROC curve. This is obtained by  
244 repeatedly classifying the susceptibility at varying thresholds and plotting each pair of TPR and FPR. Its  
245 integral or AUC is commonly used as a model diagnostic with values around 0.5 considered unsuitable,  
246 values of 1.0 to be considered ideal, and the transition between the two expressing an increase in

247 classification performance ([Hajian-Tilaki, 2013](#)).

### 248 **3.6 Stepwise GAM**

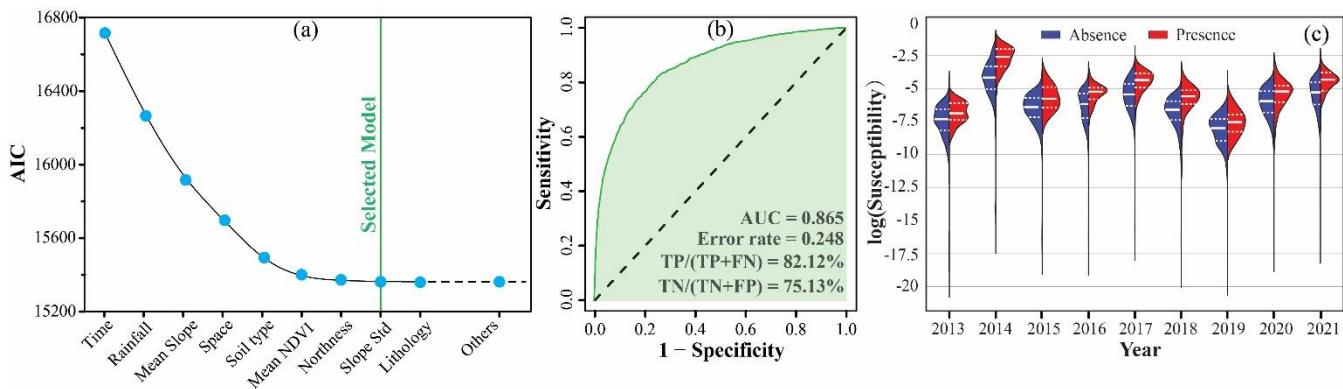
249 Covariate selection ensures an optimal set of parameters to build a given data-driven model on.  
250 Generally, several approaches can be taken to perform this task, including for instance, Ridge ([McDonald,  
251 G.C., 2009](#)) and LASSO ([Amato et al., 2019](#)) regressions, or a number of stepwise procedures ([Agostinelli,  
252 C., 2002](#)). In this study, we used a step-wise GAM approach to remove redundant and non-informative  
253 covariates. We, therefore, fitted a number of 17 individual GAMs, starting from the use of a single  
254 variable (see [Table 1](#)). From them, we selected the covariate that led to the minimum Akaike Information  
255 Criterion (AIC; [Sakamoto et al., 1986](#)) value. The process was sequentially run adding one variable at a  
256 time, solving for all combinations that would lead first to the couple of covariates with the least AIC,  
257 then to the triplet with the least AIC, and so on. We implemented this procedure in such a way that would  
258 highlight the best model, which corresponds to the situation after which the AIC has a negligible decrease  
259 even after adding new covariates.

## 260 **4 Results**

### 261 **4.1 Covariates selection and goodness-of-fit**

262 We use a forward-stepwise procedure to choose the best covariate set. Among all the tests we have  
263 run, we featured covariates used in the linear and nonlinear form and even included a few cases where we  
264 allowed for variable interactions. In [Figure 2a](#), we show an overview of some of these tests, already ranked  
265 from the highest to the lowest AIC results, and concerning the last configuration we obtained (with linear and  
266 nonlinear cases as well as interactions already pre-defined). We stress here that a stepwise selection requires  
267 a factorial combination of all the considered variables even with a single covariate configuration. Therefore,  
268 for conciseness and simplicity reasons, we report the essential information corresponding to the last test,  
269 where the minimum  $\Delta_{AIC}$  from one step to the next is reached at the inclusion of the *Slope $_{\sigma}$* , featuring each  
270 covariate as a spline effect, except *Northness $_{\mu}$*  and *Slope $_{\sigma}$*  here used linearly. Notably, we also allowed for  
271 variable interaction in the case of the *Daily maximum* and *Annual sum* of the rainfall, and for the *x* and *y*  
272 locations of the slope units. The first interaction is chosen to reflect two aspects of the rainfall effect on the  
273 yearly distribution of landslides, where the *Daily maximum* conveys the impulsive meteorological signal and  
274 the *Annual sum* conveys the overall behavior. As for the combination of the *x* and *y* locations, this is meant  
275 to ensure that proximal and far away slope units are treated differently, as prescribed for any spatial  
276 model. We also point out the fact that the minimum  $\Delta_{AIC}$  excludes the *Lithology* from the model, something

277 we interpreted because of its similarity to the *Soil type* and because the dominant landslide type in the multi-  
 278 temporal inventory corresponds to shallow failures. This particular covariate set then leads to a reference  
 279 space-time model whose goodness-of-fit is shown in Figure 2b with overall accuracies of positive and  
 280 negative cases of 82.12% and 75.13%, respectively. To these measures, the error rate of 0.248 and the  
 281 AUC of 0.87 attest for the excellent performance of the model (see, Hosmer and Lemeshow, 2000). However,  
 282 these goodness-of-fit considerations are mostly valid for the whole space-time classification process, and they  
 283 do not differentiate between the results obtained across each year constituting the whole domain. For this  
 284 reason, we opted to include Figure 2c. There, we showcased how the whole space-time domain can be  
 285 dissected on a yearly basis, providing an overview of year-specific susceptibilities against the original  
 286 presence/absence labels. In such a plot a suitable classifier would produce different probability densities for  
 287 slope units hosting landslides or not. Indeed, what we see is that across each year under consideration the  
 288 bulk of the two (presence/absence) probability distributions are quite far from each other. This in turn  
 289 indicates that our space-time model suitably discriminates stable and unstable slope units both in space  
 290 and time.

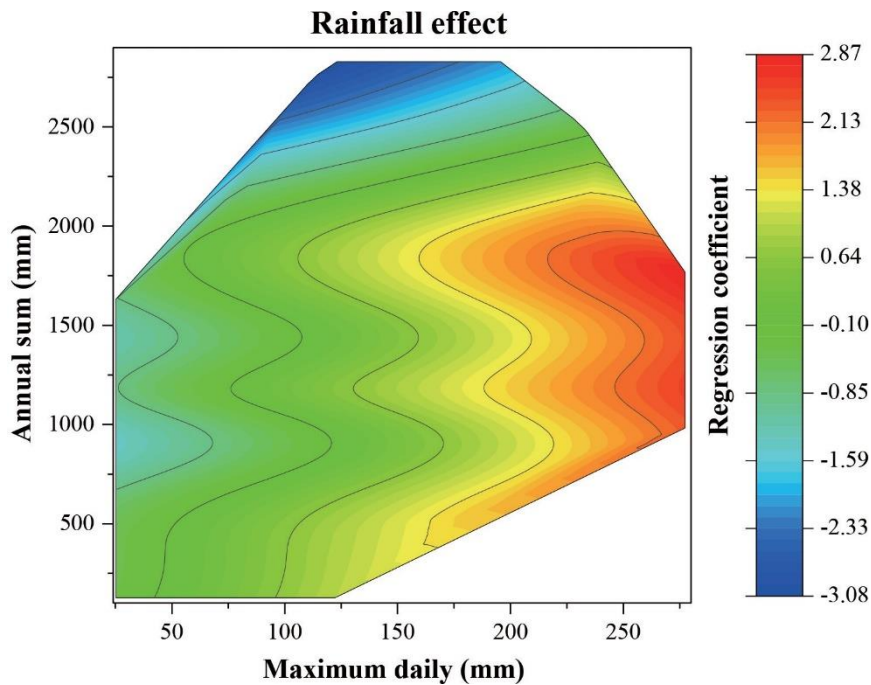


291  
 292 Figure 2: Panel (a) shows the results of the forward-stepwise covariate selection we implemented. Panel (b)  
 293 reports the corresponding goodness-of-fit measured in terms of the ROC curve and its AUC. Panel (c) fragments  
 294 on a yearly basis the overall performance overview already provided in panel b. This last panel offers a graphical  
 295 summary of the estimated susceptibility (shown in log scale for visualization purposes), plotted against the  
 296 original presence/absence data. White solid lines correspond to the mean value of the respective distributions,  
 297 whereas the width between the two white dotted lines corresponds to  $\pm 1\sigma$ .

## 298 4.2 Covariate's effects

299 Covariate effects are shown in Figures 3 and 4. The reason for this split is meant to highlight some  
 300 interesting aspects not usually explored in other landslide susceptibility contributions. In fact, Figure 3 offers  
 301 a unique view of the interaction effect between two rainfall parameters and how this combined effect  
 302 contributes to the probability of landslide occurrence in space and time. What we would like to highlight are

303 the two extremes of the regression coefficient range. The minimum regression coefficient is estimated for  
 304 large values of annual daily sum and relatively low maximum daily precipitation. As for the maximum  
 305 regression coefficients, these are obtained for large daily maximum values associated with relatively low  
 306 yearly cumulative precipitation. The way we interpret this signal is that large total rainfall data associated  
 307 with average daily maxima would correspond to meteorological conditions for which the landscape is  
 308 exposed to continuous “drizzle”. Such prolonged, low-intensity rainfall may not have the capacity to  
 309 initiate shallow landslides, which we remind here constitutes the dominant landslide type in the study  
 310 area. As for the opposite situation, we interpret the large effect brought by large daily maxima associated  
 311 with relatively low total yearly precipitation as an indicator of impulsive cloudbursts capable of releasing  
 312 large quantities of rain (up to 300mm) in a relatively short amount of time. This situation may therefore modify  
 313 the slope equilibrium rapidly forcing a pore-pressure increase and consequently leading to a decrease in the  
 314 slope stability.

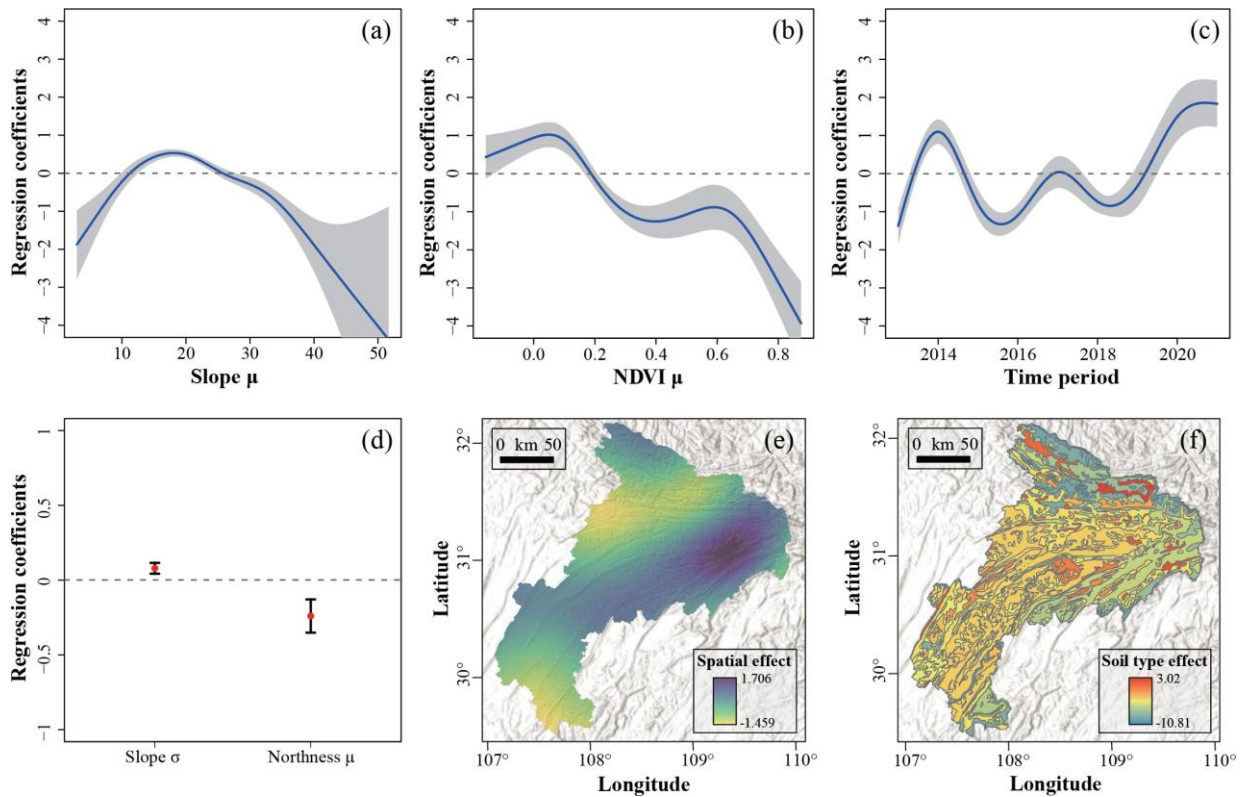


315  
 316 Figure 3: Summary of the variable interaction plot for the two rainfall indicators used in the model.

317 Moving onto a more common representation of covariate effects, in Figure 4a, we notice a spline effect in  
 318 the  $Slope_{\mu}$  negatively contributes to the spatiotemporal probability of landslide occurrence in the range  
 319 between 0 and 12 as well as 28 to 53 average degrees per slope unit. Putting things into perspective, this is  
 320 a geomorphologically reasonable result as 0°-12° are slope characteristics typical of near flat to very gentle  
 321 slopes. As for the 28°-53° range, this may correspond to slope units too steep to host any potentially unstable  
 322 soil column.

323 In Figure 4b, the  $NDVI_{\mu}$  effects appear to follow an overall negative trend, where susceptible slopes  
324 are associated with bare conditions, at best covered by sparse vegetation ( $-0.15 < NDVI_{\mu} < 0.15$ ). Higher  
325 vegetation density indicators are all associated with negative regression coefficients. Such a pattern also  
326 appears to be geomorphologically sound, for dense vegetation may interfere with the splash effect of the  
327 rain as well as increase the soil stability through the root system. The last individual spline effect is depicted  
328 in Figure 4c, where the spikes in the regression coefficients are associated with years that have also  
329 recorded a high number of landslide occurrences. Two interesting observations need to be made here, the  
330 first one being the fact that the highest spike (2021) in the regression coefficient does not correspond to  
331 the year with the largest number of failures (2014). This may be because the rainfall signal is largely  
332 capable of explaining the landslides triggered in 2014, therefore limiting the temporal effect. As for the  
333 year 2021, the rainfall does not appear to be extreme, nor in its daily maximum expression nor its yearly  
334 sum. Therefore, the model may estimate a larger regression coefficient for this period, to be potentially  
335 attributed to unobserved or latent covariate effects (see [Opitz et al., 2022](#), for further explanations).

336 Figure 4d reports the significant linear effects of  $Slope_{\mu}$  and  $Northness_{\mu}$ . The former is estimated with  
337 a positive contribution, something interpretable as a function of roughness. In fact, large variations of slope  
338 steepness within a single slope unit are indicative of rough conditions. This being said, it is also worth  
339 mentioning that the regression coefficient distribution, albeit significant, is not far away from the zero  
340 line, which implies a very limited effect overall. As for the second covariate, this marks a larger effect by  
341 comparison (the mean regression coefficient is farther away from the zero line). In turn, this implies that  
342 slopes that are facing south are the ones that are mostly associated with slope failures. Figures 4e and  
343 4f respectively show the spatial and soil type effects. What stands out the most is that the spatial effect  
344 contributes by promoting unstable SUs to the very south, and in the northern sector where the pattern  
345 shows a NE-SW direction. Interestingly, this is also the main direction of the tectonic lineaments present  
346 in the area. Conversely, soil control on slope stability is much more spatially complex. For reasons of  
347 conciseness, we only report here the two major pedological classes contributing to the SU classification.  
348 Specifically, gravelly sands with a loamy component are associated with the largest regression coefficient  
349 ( $\beta = 3.02$ ). Conversely, black soils negatively contribute to the space-time susceptibility ( $\beta = -10.16$ ).



350

351

352

353

354

355

### 356 4.3 Space-time predictive performance

357

358

359

360

361

362

363

364

365

366

367

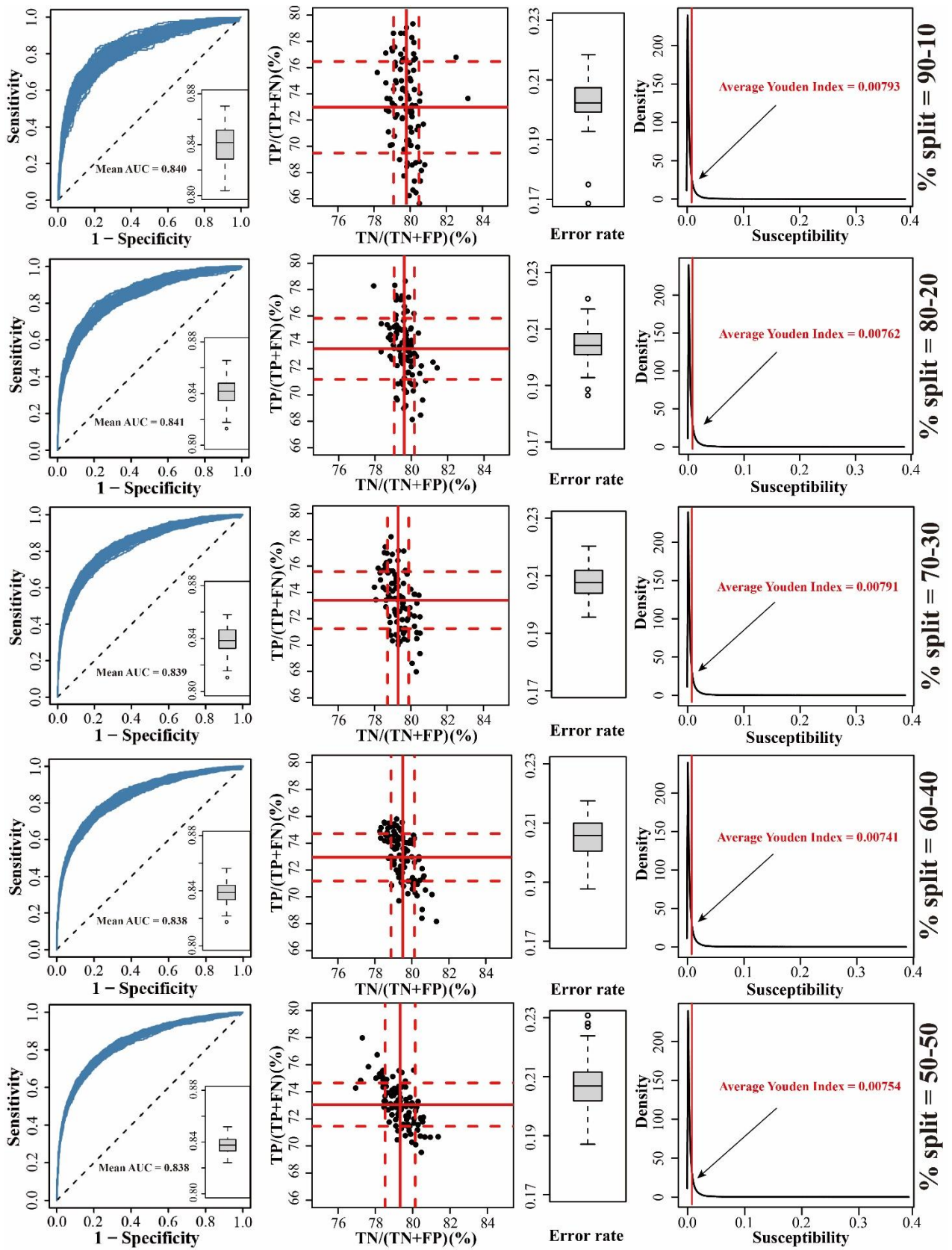
368

Before presenting the results of our space-time random cross-validation (RCV), we would like to remind the readers of an important aspect often neglected in the literature. We initially recall that a validation procedure should highlight the model's capacity to suitably predict data that has not been featured as part of the calibration phase. However, this is not the only requirement of a robust performance assessment. Traditionally, one often assumes that the structure of the data may carry some degree of spatial autocorrelation and that in turn, this may optimistically bias the final performance. This is why [Brenning \(2012\)](#) prescribes spatial cross-validation routines, and [Roberts et al. \(2017\)](#) recommend space-time cross-validation routines, because, through these techniques, one can ensure any dependence structure in the data to be broken down, allowing for an unbiased predictive performance assessment. However, [\(Wadoux et al., 2021\)](#) recently challenged such statements, demonstrating that random cross-validation produces negligible differences as compared to spatial cross-validation routines. Considering these two radically opposite positions, in this work we opted for an RCV that we progressively pushed towards more

369 significant sample removals. In such a way, we would both equip our model with an RCV but also  
370 ensure that any spatiotemporal autocorrelation would be progressively weakened, allowing for a suitable  
371 assessment.

372 These results are shown in Figure 5, where each row represents a different percentage split in the  
373 RCV. Each column, represents a different aspect of the performance assessment, starting from reporting the  
374 cutoff independent assessment summarized via the ROC curves obtained for each of the 100 iterations.  
375 The subsequent two columns correspond to the accuracy (or confusion) plot for the positives and  
376 negatives, as well as the error rate box plots. Both metrics are obtained using a probability cutoff  
377 corresponding to the Youden index, reported in the fourth column. What stands out the most is that the  
378 performance is extremely stable. Irrespective of the portion of the data that we randomly extract for  
379 validation, the model performance essentially stays the same. The AUC values maintain an average very  
380 close to 0.84. The accuracy of the model in predicting absence cases essentially stays between 79% and 80%,  
381 whereas the same for the present instances is confined between 72% and 74%. This is also reflected in the  
382 error rate, being stable at around 0.21. These are important considerations that support our model not only  
383 as an explanatory tool but also as a robust predictive one.





384  
 385  
 386

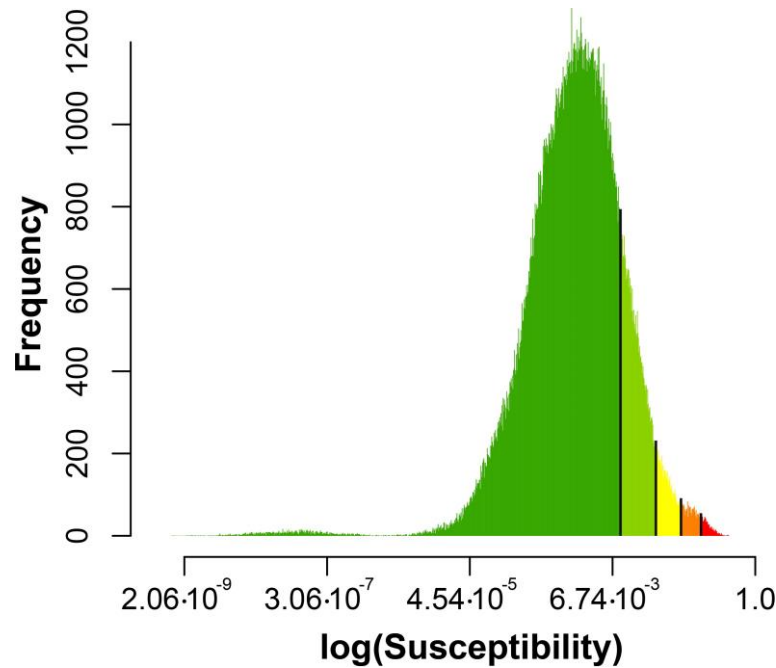
Figure 5: Random cross-validation performance summary of ROC, confusion, error ratio, and average Youden index distribution in the 90/10, 80/20, 70/30, 60/40, and 50/50 selection ratios.

387 **4.4 Susceptibility mapping**

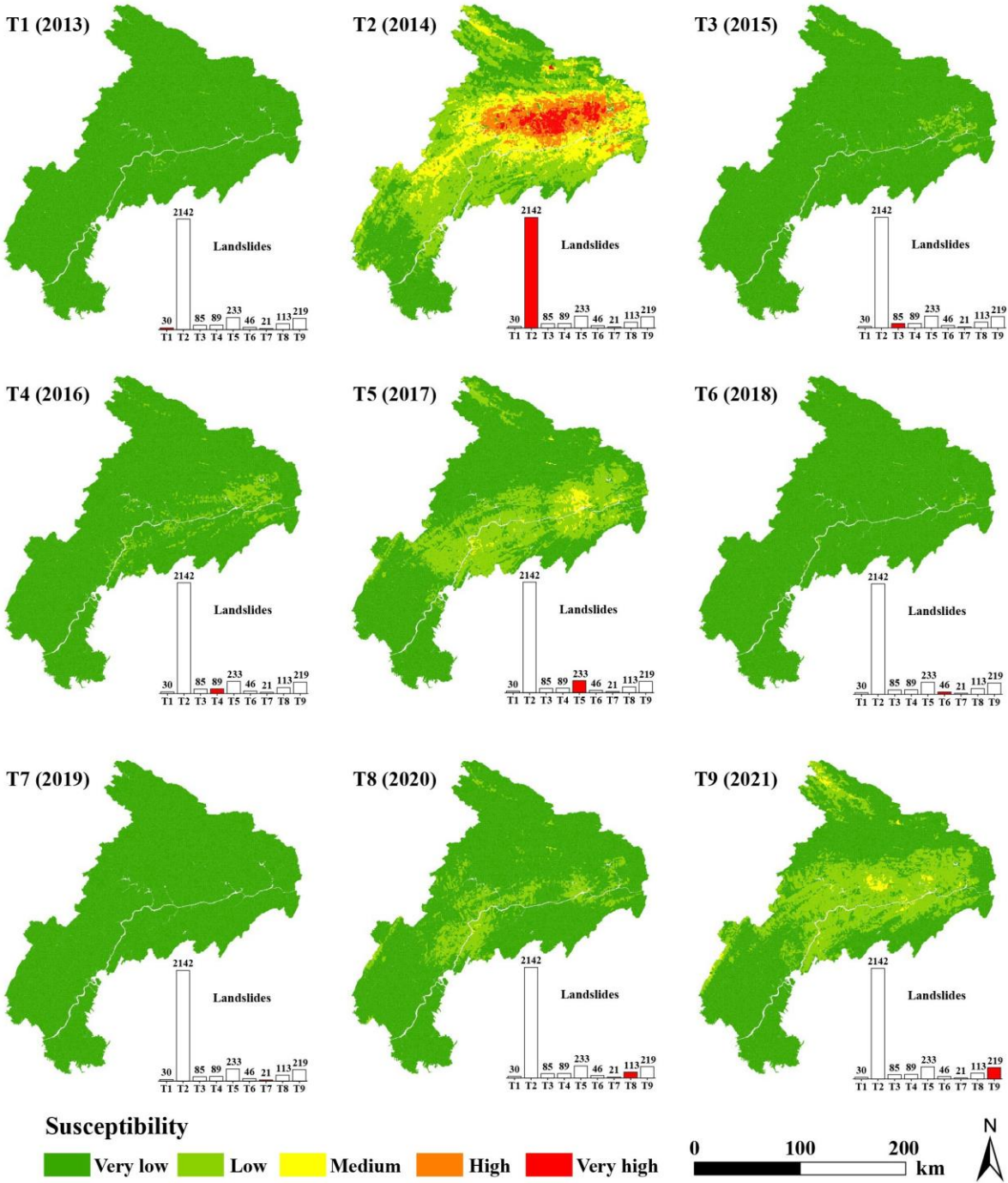
388 Having demonstrated the predictive capacity of our space-time susceptibility model, in this section,  
389 we translate the model results into maps. However, susceptibility maps need to undergo a further  
390 processing step where the continuous spectrum of probability values is binned in a number of classes.  
391 Therefore, finding suitable breaks corresponding to each class limit is required. Here we present this step in  
392 Figure 6, where all the space-time probability domain is classified according to five classes following the  
393 Jenks method (North, 2009). We recall here that this method starts from a pre-defined number of classes and  
394 finds the cutoffs that minimize the intra-class variances.

395 The very same probability cutoffs have been used to plot the nine separate susceptibility maps shown in  
396 Figure 7. There one can appreciate the flexibility of our space-time model in mimicking the overall yearly  
397 landslide frequency (see nested bar plots) in the level associated with each susceptibility map.

398 This is particularly evident for the second map where 2142 out of 2978 occurred just in the year  
399 2014. This level of consistency justifies the use of our space-time model for cartographic purposes  
400 and the next section will be dedicated to the generation of future scenarios using a simulation approach.



401  
402 Figure 6: Jenks classification of the spatiotemporal distribution of fitted susceptibility values from 2013 to 2021.  
403 We opted to plot the probability values in logarithmic scale because the original scale is very heavy-tailed, making  
404 it difficult to graphically represent it.



405

406

407

Figure 7: Landslide susceptibility map for the year from 2013 to 2021. Continuous susceptibility values are grouped into five classes with Jenks classification.

408

**4.5 Future risk forecasting**

409

Generalizing data-driven susceptibility models is almost done exclusively in the spatial dimension, through a procedure commonly referred to as model transferability (Petschko et al., 2014; Wang et al., 2022b). Conversely, here we transfer our model in time using a plug-in simulation approach (see Lombardo and Tanyas, 2020). In other words: 1) we solve the predictive equation we obtained, 2) we keep all the

410

411

412

413 covariates as they are except the two rainfall parameters, 3) we remove the rainfall data estimated for the  
414 years 2013-2021, and 4) introduce the rainfall projected for the years 2022-2030. But, as interesting as such  
415 a procedure may be, it still does not convey any information on the expected risk local communities  
416 may be exposed to. For this reason, not only we simulated future landslide susceptibility scenarios, but  
417 we also collected two more exposure parameters in the form of future built-up areal extent ( $m^2$ ) and the  
418 future number of inhabitants. A description of both parameters can be found in [Lepetit et al. \(2023\)](#) and  
419 they can be accessed at <https://ghsl.jrc.ec.europa.eu/download.php?ds=pop>.

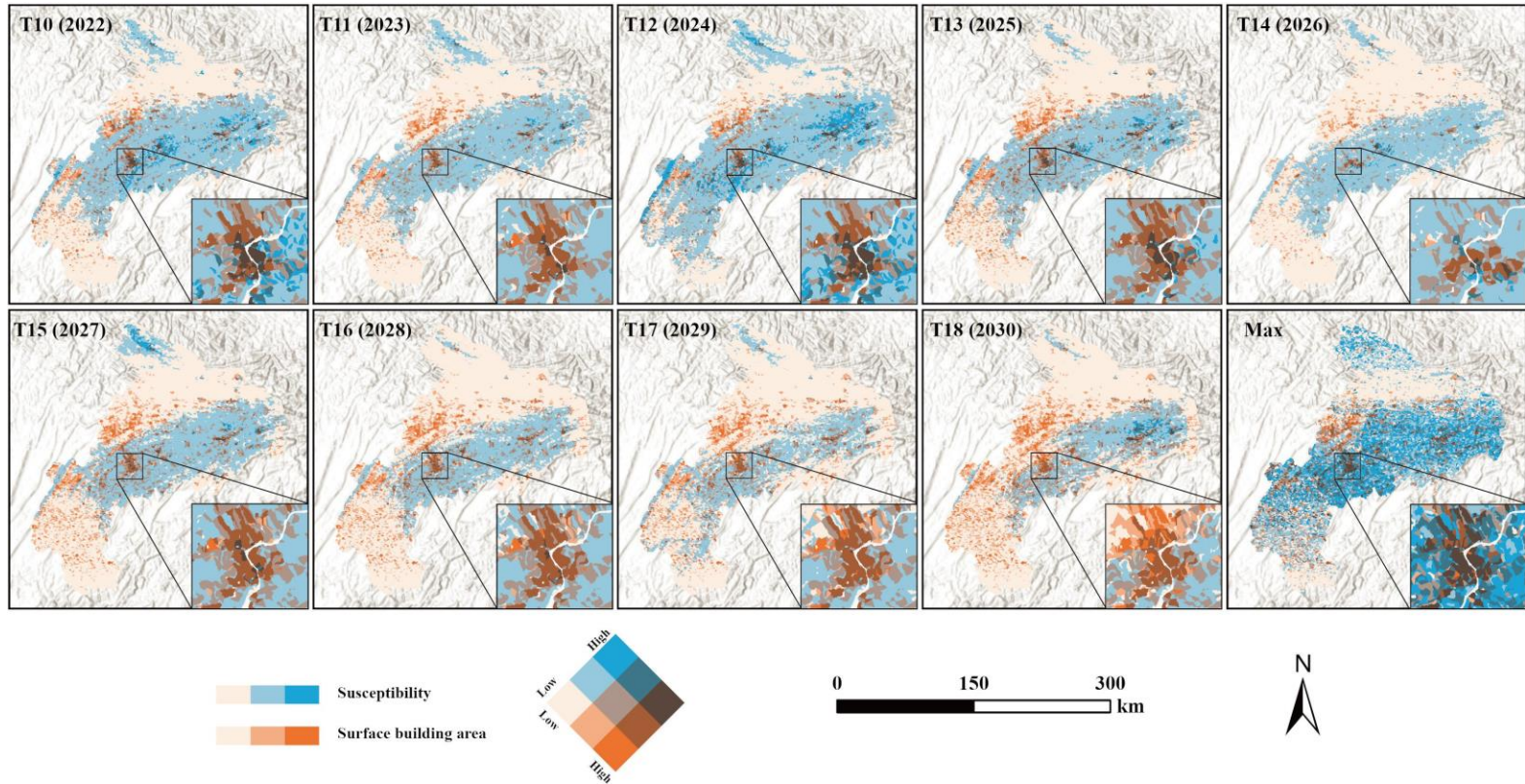
420 The combination of estimated susceptibility, together with the two exposure parameters is shown in  
421 Figures 8 and 9. In the first case, one cannot assume the information to fully reflect the risk because it is  
422 not possible to assign a specific vulnerability curve to a generic layer reporting the expected built-up area  
423 distribution. However, if one would assume the vulnerability = 1, then the combination of the two layers  
424 would indeed depict the risk to the building and infrastructure. We recall here that the reference natural hazard  
425 corresponds to rapid landslides, and therefore, hypothesizing that a given built-up area would be hit by a  
426 fast-moving mass should not be an unreasonable assumption. Conversely, this issue does not affect the  
427 exposure data of the local population, which indeed would incur losses if they would find themselves in the  
428 path of a theoretical debris flow.

429 Going back to the individual figures' content, the two landslide risk maps highlight slightly different areas  
430 potentially requiring further attention. Built-up areas under the most threat from landslides are mostly  
431 located in the central sector of the northeast of Chongqing, irrespective of the year under consideration.  
432 As for the population, the same densely inhabited area appears to be likely exposed to landslide  
433 occurrences. However, right eastward of it, some interesting spatiotemporal patterns can be seen with the  
434 combination of highly likely landslide occurrence probabilities and expected inhabitants generating high-  
435 risk patches in the zoomed-in part of the maps.

436 We can also see that the worst-case risk scenarios determined by the susceptibility (lowest right panels in  
437 Figures 8 and 9) produce two slightly different patterns with the built-up area being more subjected to  
438 landslide risk as compared to the local expected population. One would expect the two exposure  
439 parameters to be mostly correlated. Therefore, such differences may be mostly interpreted with part of  
440 the built-up area being allocated to industrial activities and hence, to a lesser population density.

441 To confirm this interpretation, further analyzed the two exposure parameters and showed their  
442 spatiotemporal characteristics in Figure 10. There, one can notice that panel (a) projects an increase in  
443 expected built-up with time (from  $\sim 150 \text{ km}^2$  between 2022 and 2024 to  $\sim 200 \text{ km}^2$  between 2025 and  
444 2029, and up to  $\sim 240 \text{ km}^2$ ). Conversely, the population is projected to slightly decay, starting from

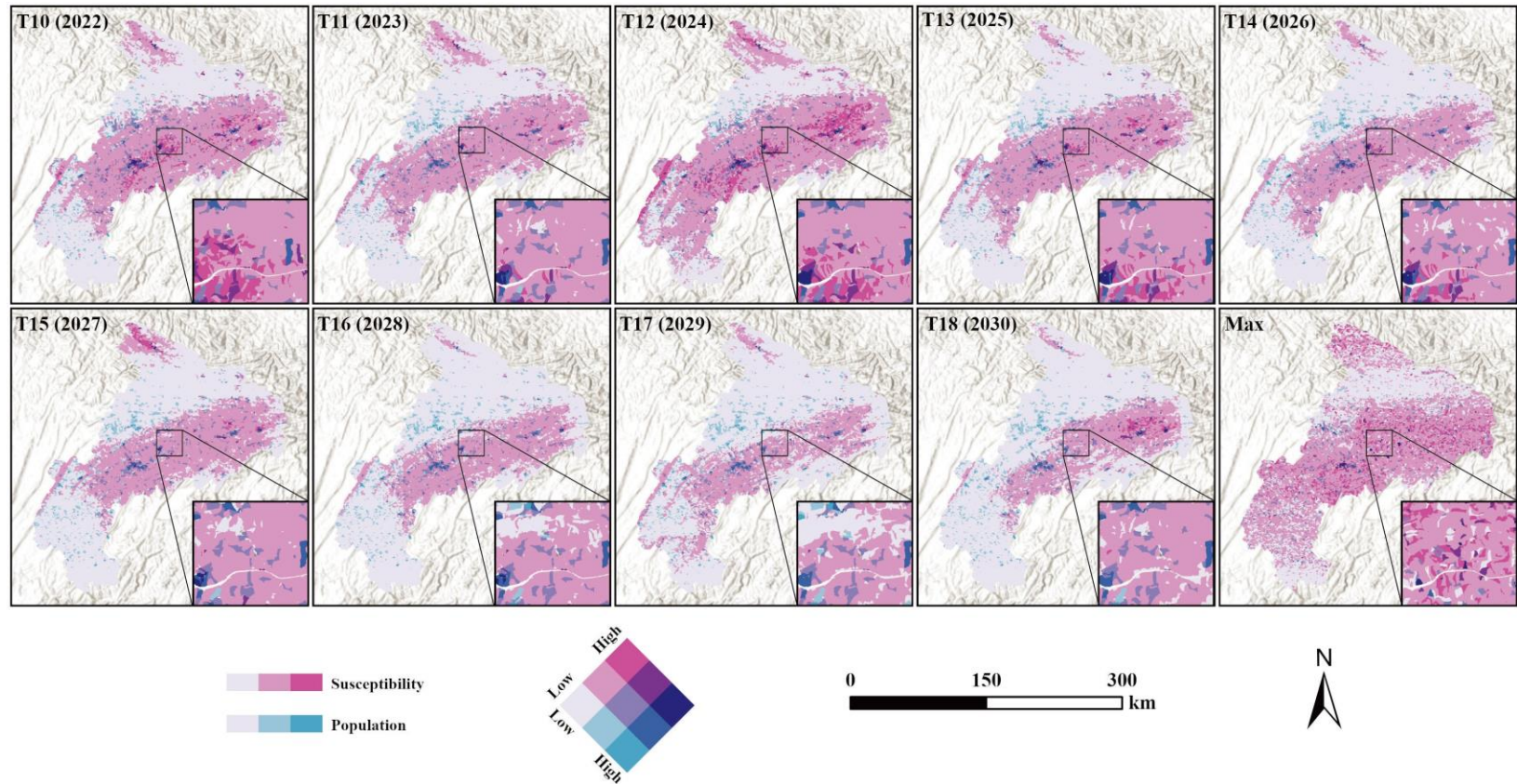
445  
446  
447



448  
449  
450  
451  
452  
453  
454  
455

Figure 8: Impact-based scenarios obtained by combining landslide occurrence probability and built-up area projections. The first nine panels depict the yearly variation of landslide susceptibility, whereas the built-up area scenarios vary on a 5-yearly basis. The last panel corresponds to the worst combined scenario (max susceptibility and associated building distribution) out of the 9 projected years.

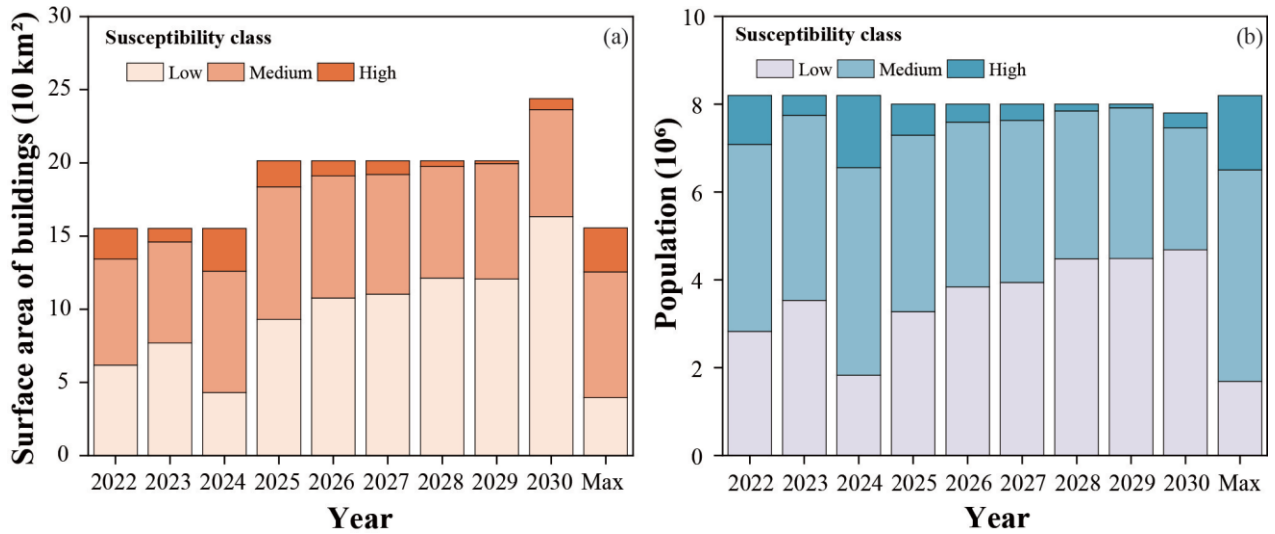
456  
457



458  
459  
460  
461

Figure 9: Impact-based scenarios obtained by combining landslide occurrence probability and the number of inhabitants projections. The first nine panels depict the yearly variation of landslide susceptibility, whereas the population scenarios vary on a 5-yearly basis. The last panel corresponds to the worst combined scenario (max susceptibility and associated population distribution) out of the 9 projected years.

462 around 8.2 million inhabitants in 2022 and reaching around 7.8 million in 2030. The same plots can be  
 463 used to assess the goodness of local master plans. In fact, the proportion of built-up areas and populations  
 464 in 2022 falls in both cases within a low susceptibility class much smaller as compared to the combination  
 465 of medium and high classes. However, most of the built-up areas and inhabitants would be associated  
 466 with the low susceptibility class in 2030.



467  
 468 Figure 10: Distribution of projected built-up areas (a) and populations associated with specific susceptibility  
 469 classes over the 9 projected years. The last stacked bar plot reports the two parameters for the respective cases  
 470 where the space-time susceptibility has reached its maximum value per slope unit.

## 471 5 Discussion

472 This section is dedicated to scrutinizing our modeling protocol and its results, highlighting potential  
 473 strengths and weaknesses. For this reason, below we dedicate two separate sections to the respective  
 474 considerations.

### 475 5.1 Supporting arguments

476 Space-time susceptibility modeling is still largely unexplored (Reichenbach et al., 2018). Most of  
 477 the current literature still uses landslide inventories where the temporal information is missing or left unused.  
 478 For this reason, our modeling protocol already presents an example of state-of-the-art data-driven solutions  
 479 for landslide spatiotemporal prediction. And even in the framework of an already limited literature, in this  
 480 work, we further nested a number of sub-experiments that by themselves offer “food for thought” for  
 481 landslide practitioners. For instance, we introduced a first attempt to explore the rainfall effect in the  
 482 form of a variable interaction term (see Figure 3). This allowed us to dive into how the combination of yearly  
 483 rainfall parameters influences the likelihood of landslide occurrences in space and time. Currently, the use of  
 484 variable interaction terms in the landslide literature is mostly confined to cases where one of the two

485 covariates is continuous and the second one is categorical. For instance, [Brenning et al. \(2015\)](#) used this  
486 idea to investigate the effect of road distances per lithological class in Ecuador. The only examples where  
487 a two-variable interaction has been previously used to explore precipitation effects can be found in [Goetz  
488 et al. \(2015\)](#), where the authors explore how precipitation intensities contribute to landslide occurrence  
489 probabilities at varying levels of forest cover. The same idea has been recently featured in [Johnston et al.  
490 \(2021\)](#) by allowing precipitation to interact with three different land use types. Here, we present an  
491 alternative where two aspects of the same meteorological process can interact and be brought into the  
492 model as a unique effect. This could be interesting beyond the context of landslide susceptibility.  
493 Specifically, we envision this idea as a useful tool in landslide early warning systems, where the modeling  
494 target is usually determined by intensity-duration relationships (e.g., [Rossi et al., 2012](#)).

495 Another nested experiment corresponds to the use of an RCV routine where a larger proportion of  
496 the space-time data are progressively taken away from the calibration phase and merged into the prediction  
497 subset. The common practice mostly corresponds to a single fixed data split (e.g., [Rossi et al., 2010](#)) and  
498 the model sensitivity to the proportion of data allocated to the fitting and testing phases is hardly  
499 acknowledged. Here, we touch on this subject by exploring the results produced by 100 RCVs obtained  
500 from five separate schemes, moving from a 90/10 to a 50/50 split. Interestingly, the last data split takes  
501 away a significant amount of data without being followed by a proportional loss in predictive performance.  
502 This attests to a robust model, whose stability is reached even when potential space-time autocorrelation  
503 effects are necessarily broken at this level of data-removal. Another strength we recognize is using a space-  
504 time model for scenario-making purposes. In landslide susceptibility studies, this has been explored in a  
505 limited number of contributions. For instance, [Steger et al. \(2023\)](#) take a similar stance for predicting  
506 landslides on a daily time step. Recently, [Knevels et al. \(2023\)](#) make use of an analogous simulations  
507 framework by fitting a binomial GAM and generating landslide scenarios for a complex combination of  
508 future environmental (climate, and land use projections) conditions in Austria. Here, we take a simpler  
509 approach by simulating only the rainfall projections. However, we extend the research to combine exposure  
510 information to generate risk scenarios. This is also an area where the landslide literature is explored to a  
511 lesser extent as compared to the amount of pure landslide susceptibility studies. Valuable contributions on  
512 landslide risk do exist, and a number of milestones can be found in the work laid out by ([Guzzetti, 2000](#);  
513 [Corominas et al., 2014](#)). However, they are mostly confined to current risk assessments and rarely feature  
514 elements of predictive modeling ([Malek et al., 2015](#); [Rossi et al., 2019](#)).

## 515 **5.2 Opposing arguments**

516 A number of limitations affect the analyses we present here. The most evident is in the way we



517 generate landslide occurrence probability projections. In fact, we simulate by changing only the rainfall  
518 patterns. This implies that all the other predictors are kept constant even in future years. This assumption  
519 may be reasonable for covariates that typically exhibit a low rate of temporal change such as the DEM  
520 derivatives. However, it may be considered a limitation in the case of the NDVI. However, we did not  
521 have access to vegetation density projections. This being said, the rate at which the NDVI changed  
522 through time across the study area appears to be minor and therefore, we also assume this to produce a  
523 negligible bias. Also, what we are proposing here is an approach to model space-time risk, and future  
524 work can be further extended to account for the issues we noted during the present experiment. Another  
525 potential source of bias may reside in the difference in spatial resolution between different rainfall  
526 products. In fact, if the native rainfall information is expressed daily both at the level of the local rain  
527 gauge network and in the climate projections, the same cannot be said in the spatial dimension. The rain  
528 gauges network in the northeast sector of Chongqing is particularly dense, with the maximum distance  
529 between two neighboring stations being approximately 20km whereas the average distance is 7.2 km.  
530 However, the raw rainfall projections have a native resolution of approximately 26 km × 26km. This is  
531 to stress that the capacity at which the precipitation signal is represented in the fitted model (although  
532 interpolated) is higher than the rainfall counterpart used for the simulation phase (although downscaled).  
533 This may potentially represent an issue in the uncertainty propagation from one modeling step to the next  
534 and future research direction may involve an intermediate phase where a bias-reduction step will be  
535 required to minimize the difference between observed and predicted rainfall.

536 Moving toward the risk component of the present research, some limitations also apply to the  
537 exposure data. In fact, the raw projections are based on a five-year time step. As a result, our yearly  
538 susceptibility scenarios vary at a higher frequency compared to the built-up area and population layers.  
539 This being said, it is reasonable for this to be the case because landslide-prone conditions may be indeed  
540 quite different from one year to the next, whereas the urban fabric and its inhabitants vary at a lower  
541 rate. Nevertheless, an ideal situation would correspond to a one-to-one correspondence, and future efforts  
542 may be dedicated to producing in-house exposure projections at a higher temporal resolution.

## 543 **6 Concluding remarks**

544 This contribution presents an analytical protocol where the landslide risk projections are obtained  
545 as a combination of simulated susceptibility estimates and two separate exposure parameters (built-up  
546 areas and local population). This experimental design may constitute the foundation on urban planners  
547 to base their decisions on because we integrate two fundamental aspects in risk assessments: spatial and  
548 temporal probabilities together with exposure data. We stress that the model we present is just a prototype

549 and further improvements are required to fulfill the risk definition. In fact, to complete the landslide  
550 hazard assessment, the spatiotemporal probabilities need to be associated with the expected landslide  
551 intensities. To accommodate for this, we currently exploring a class of models where landslide areas can  
552 be jointly predicted in space and time together with the susceptibility. Another requirement that is  
553 prohibitive to get access to for such a large area corresponds to vulnerability curves, at least for the major  
554 infrastructure and building of interest. Even in this case, we are collaborating with local institutes to  
555 generate vulnerability data and their potential variations in space and time.

556 Overall, we believe this type of modeling framework holds great potential in the framework of  
557 landslide prediction at large. In fact, its structure can be flexibly adapted to local spatial and daily  
558 temporal domains offering solutions in line with early warning systems. And, if adapted to regional  
559 spatial and yearly temporal domains, it can offer solutions in line with scenario projections. The addition  
560 of the exposure components ensures the extension of the probabilistic results towards an integrated risk  
561 modeling approach, whose full potential may be unlocked once urban-finance data will be collected and  
562 analyzed for loss quantification.

### 563 **Author contributions statement**

564 **Luigi Lombardo** has devised the experiment, written the manuscript, and produced the scientific  
565 illustrations. **Tengfei Wang** has pre-processed the data, run all the analyses, produced the scientific  
566 illustrations, and written the manuscript. **Ashok Dahal** has helped with computing the rainfall projections  
567 and writing the manuscript and figures. **Zhice Fang** has helped with the model implementation. **Cees van**  
568 **Westen** has taken part in different stages of the experiment, mainly contributing to the discussion and the  
569 critical revision of the research idea. **Kunlong Yin** is the data provider and formal doctoral supervisor  
570 of **Tengfei Wang**.

### 571 **Acknowledgement**

572 This research was supported by the National Natural Science Foundation of China – Young Scientist  
573 Funds (No.42207174). The first author wishes to thank the China Scholarship Council (CSC) for funding  
574 his research period at the University of Twente.

### 575 **References**

576 Abella, E. C. and Van Westen, C. (2007) Generation of a landslide risk index map for Cuba using spatial  
577 multi-criteria evaluation. *Landslides* 4(4), 311–325.  
578 Agostinelli, C., 2002. Robust stepwise regression. *Journal of Applied Statistics*, 29(6), pp.825-840.

579 Ahmed, B. (2021) The root causes of landslide vulnerability in Bangladesh. Landslides **18**(5), 1707–1720.

580 Alvioli, M., Marchesini, I., Reichenbach, P., Rossi, M., Ardizzone, F., Fiorucci, F and Guzzetti,  
581 F. (2016) Automatic delineation of geomorphological slope units with r. slopeunits v1.0 and their  
582 optimization for landslide susceptibility modeling. Geoscientific Model Development **9**(11), 3975–3991.

583 Amato, G., Eisank, C., Castro-Camilo, D. and Lombardo, L., 2019. Accounting for covariate  
584 distributions in slope-unit-based landslide susceptibility models. A case study in the alpine  
585 environment. Engineering geology, 260, p.105237.

586 Babak, O., Deutsch, C.V., 2009. Statistical approach to inverse distance interpolation. Stochastic  
587 Environmental Research and Risk Assessment **23**, 543–553.

588 Beck, N., Katz, J.N., Tucker, R., 1998. Taking time seriously: Time-series-cross-section analysis with a  
589 binary dependent variable. American Journal of Political Science **42**, 1260–1288.

590 Brenning, A. (2012) Spatial cross-validation and bootstrap for the assessment of prediction rules in remote  
591 sensing: The r package sperrorest. In 2012 IEEE international geoscience and remote sensing symposium,  
592 pp. 5372–5375.

593 Brenning, A., 2008. Statistical geocomputing combining R and SAGA: The example of landslide  
594 susceptibility analysis with generalized additive models. Hamburger Beiträge zur Physischen  
595 Geographie und Landschaftsökologie **19**, 410.

596 Brenning, A., Schwinn, M., Ruiz-Páez, A. and Muenchow, J. (2015) Landslide susceptibility near highways  
597 is increased by 1 order of magnitude in the Andes of southern Ecuador, Loja province. Natural  
598 Hazards and Earth System Sciences **15**(1), 45–57.

599 Budimir, M., Atkinson, P. and Lewis, H. (2015) A systematic review of landslide probability mapping  
600 using logistic regression. Landslides **12**(3), 419–436.

601 Calcaterra, D., Di Martire, D., Palma, B. and Parise, M. (2010) Assessing landslide risk through unique  
602 condition units.

603 Carrara, A. (1988) Drainage and divide networks derived from high-fidelity digital terrain models. In  
604 Quantitative analysis of mineral and energy resources, pp. 581–597. Springer.

605 Carrara, A., Cardinali, M., Detti, R., Guzzetti, F., Pasqui, V. and Reichenbach, P. (1991) Gis techniques  
606 and statistical models in evaluating landslide hazard. Earth surface processes and landforms **16**(5),  
607 427–445.

608 Chen, S., Yan, Y., Liu, G., Fang, D., Wu, Z., He, J. and Tang, J. (2019) Spatiotemporal characteristics  
609 of precipitation diurnal variations in Chongqing with complex terrain. Theoretical and Applied  
610 Climatology **137**, 1217–1231.

611 Conoscenti, C., Rotigliano, E., Cama, M., Caraballo-Arias, N. A., Lombardo, L. and Agnesi, V. (2016)  
612 Exploring the effect of absence selection on landslide susceptibility models: A case study in Sicily,  
613 Italy. Geomorphology **261**, 222–235.

614 Corominas, J., van Westen, C., Frattini, P., Cascini, L., Malet, J.-P., Fotopoulou, S., Catani, F., Van Den  
615 Eeckhaut, M., Mavrouli, O., Agliardi, F. et al. (2014) Recommendations for the quantitative analysis  
616 of landslide risk. Bulletin of engineering geology and the environment **73**, 209–263.

617 Cressie, N. (1988) Spatial prediction and ordinary kriging. Mathematical geology **20**, 405–421.

618 Dai, F., Lee, C. F. and Ngai, Y. Y. (2002) Landslide risk assessment and management: an overview.  
619 Engineering geology **64**(1), 65–87.

620 Emberson, R., Kirschbaum, D. and Stanley, T. (2020) New global characterisation of landslide exposure.  
621 Natural Hazards and Earth System Sciences **20**(12), 3413–3424.

622 Fang, Z., Wang, Y., Peng, L. and Hong, H. (2020) Integration of convolutional neural network and  
623 conventional machine learning classifiers for landslide susceptibility mapping. Computers &  
624 Geosciences **139**, 104470.

625 Fluss, R., Faraggi, D., Reiser, B., 2005. Estimation of the Youden Index and its associated cutoff point.  
626 Biometrical Journal: Journal of Mathematical Methods in Biosciences **47**, 458–472.

627 Galli, M. and Guzzetti, F. (2007) Landslide vulnerability criteria: a case study from Umbria, Central  
628 Italy. Environmental management **40**(4), 649–665.

629 Glade, T., Anderson, M. G. and Crozier, M. J. (2005) Landslide hazard and risk. Volume **807**. Wiley  
630 Online Library.

631 Goetz, J., Guthrie, R. and Brenning, A. (2015) Forest harvesting is associated with increased landslide  
632 activity during an extreme rainstorm on Vancouver Island, Canada. Natural Hazards and Earth  
633 System Sciences **15**(6), 1311–1330.

634 Gong, P., Chen, B., Li, X., Liu, H., Wang, J., Bai, Y., Chen, J., Chen, X., Fang, L., Feng, S. et al. (2020)  
635 Mapping essential urban land use categories in China (EULUC-China): Preliminary results for 2018.  
636 Science Bulletin **65**(3), 182–187.

637 Guzzetti, F. (2000) Landslide fatalities and the evaluation of landslide risk in Italy. Engineering Geology  
638 **58**(2), 89–107.

639 Hajian-Tilaki, K., 2013. Receiver operating characteristic (ROC) curve analysis for medical diagnostic  
640 test evaluation. Caspian journal of internal medicine **4**, 627.

641 Hastie, T., Tibshirani, R., 1987. Generalized additive models: some applications. Journal of the American  
642 Statistical Association **82**, 371–386.

643 Hastie, T.J., 2017. Generalized additive models, in: *Statistical Models in S*. Routledge, pp. 249–307.

644 Hosmer, D. W. and Lemeshow, S. (2000) Applied Logistic Regression. Second edition. New York:  
645 Wiley.

646 Ihaka, R., Gentleman, R., 1996. R: a language for data analysis and graphics. Journal of computational  
647 and graphical statistics **5**, 299–314.

648 Jasiewicz, J. and Stepinski, T. F. (2013) Geomorphons—a pattern recognition approach to classification  
649 and mapping of landforms. Geomorphology **182**, 147–156.

650 Jenson, S. K. and Domingue, J. O. (1988) Extracting topographic structure from digital elevation data  
651 for geographic information system analysis. Photogrammetric engineering and remote sensing  
652 **54**(11), 1593–1600.

653 Johnston, E. C., Davenport, F. V., Wang, L., Caers, J. K., Muthukrishnan, S., Burke, M. and Diffenbaugh,  
654 N. S. (2021) Quantifying the effect of precipitation on landslide hazard in urbanized and non-  
655 urbanized areas. Geophysical Research Letters **48**(16), e2021GL094038.

656 Kaynia, A., Papatoma-Köhle, M., Neuhäuser, B., Ratzinger, K., Wenzel, H. and Medina-Cetina, Z.  
657 (2008) Probabilistic assessment of vulnerability to landslide: application to the village of  
658 Lichtenstein, Baden-Württemberg, Germany. Engineering Geology **101**(1-2), 33–48.

659 Knevels, R., Petschko, H., Proske, H., Leopold, P., Mishra, A. N., Maraun, D. and Brenning, A. (2023)  
660 Assessing uncertainties in landslide susceptibility predictions in a changing environment (Styrian Basin,  
661 Austria). Natural Hazards and Earth System Sciences **23**(1), 205–229.

662 Lateltin, O., Haemmig, C., Raetzo, H. and Bonnard, C. (2005) Landslide risk management in  
663 Switzerland. Landslides **2**(4), 313–320.

664 Lepetit, Q., Vigié, V. and Liotta, C. (2023) A gridded dataset on densities, real estate prices, transport,  
665 and land use inside 192 worldwide urban areas. Data in Brief **47**, 108962.

666 Li, B., Gao, Y., Yin, Y., Wan, J., He, K., Wu, W. and Zhang, H. (2022) Rainstorm-induced large-scale  
667 landslides in Northeastern Chongqing, China, August 31 to September 2, 2014. Bulletin of  
668 Engineering Geology and the Environment **81**(7), 271.

669 Li, Y., Liu, C. and Yuan, X. (2009) Spatiotemporal features of soil and water loss in Three Gorges  
670 Reservoir Area of Chongqing. Journal of Geographical Sciences **19**(1), 81–94.

671 Lima, P., Steger, S. and Glade, T. (2021) Counteracting flawed landslide data in statistically based  
672 landslide susceptibility modelling for very large areas: a national-scale assessment for Austria.  
673 Landslides **18**(11), 3531–3546.

674 Lima, P., Steger, S., Glade, T. and Murillo-García, F. G. (2022) Literature review and bibliometric

675 analysis on data-driven assessment of landslide susceptibility. Journal of Mountain Science  
676 **19**(6), 1670–1698.

677 Lombardo, L., Bakka, H., Tanyas, H., van Westen, C., Mai, P. M. and Huser, R. (2019) Geostatistical  
678 modeling to capture seismic-shaking patterns from earthquake-induced landslides. Journal of  
679 Geophysical Research: Earth Surface **124**(7), 1958–1980.

680 Lombardo, L., Opitz, T., Ardizzone, F., Guzzetti, F. and Huser, R. (2020) Space-time landslide predictive  
681 modelling. Earth-Science Reviews p. 103318.

682 Lombardo, L., Saia, S., Schillaci, C., Mai, P. M. and Huser, R. (2018) Modeling soil organic carbon with  
683 Quantile Regression: Dissecting predictors' effects on carbon stocks. Geoderma **318**, 148–159.

684 Lombardo, L. and Tanyas, H. (2020) Chrono-validation of near-real-time landslide susceptibility models  
685 via plug-in statistical simulations. Engineering Geology **278**, 105818.

686 Luo, H., Zhang, L., Zhang, L., He, J. and Yin, K. (2023) Vulnerability of buildings to landslides: The  
687 state of the art and future needs. Earth-Science Reviews p. 104329.

688 Luo, L., Lombardo, L., van Westen, C., Pei, X. and Huang, R. (2021) From scenario-based seismic hazard  
689 to scenario-based landslide hazard: rewinding to the past via statistical simulations. Stochastic  
690 environmental research and risk assessment pp. 1–22.

691 Malek, Ž., Boerboom, L. and Glade, T. (2015) Future forest cover change scenarios with implications  
692 for landslide risk: an example from Buzau Subcarpathians, Romania. Environmental Management **56**,  
693 1228–1243.

694 McDonald, G.C., 2009. Ridge regression. Wiley Interdisciplinary Reviews: Computational  
695 Statistics, 1(1), pp.93-100.

696 Meijerink, A. (1988) Data acquisition and data capture through terrain mapping unit. ITC Jour. **1**, 23–  
697 24.

698 Mondini, A. C., Guzzetti, F. and Melillo, M. (2023) Deep learning forecast of rainfall-induced shallow  
699 landslides. Nature Communications **14**(1), 2466.

700 Nocentini, N., Rosi, A., Segoni, S., Fanti, R., et al. (2023) Towards landslide space-time forecasting  
701 through machine learning: the influence of rainfall parameters and model setting. Frontiers in Earth  
702 Science **11**, 1–20.

703 North, M. A. (2009) A method for implementing a statistically significant number of data classes in the  
704 Jenks algorithm. In 2009 Sixth International Conference on Fuzzy Systems and Knowledge  
705 Discovery, volume **1**, pp. 35–38.

706 Opitz, T., Bakka, H., Huser, R. and Lombardo, L. (2022) High-resolution Bayesian mapping of landslide

707 hazard with unobserved trigger event. The Annals of Applied Statistics **16**(3), 1653–1675.

708 Ozturk, U., Pittore, M., Behling, R., Roessner, S., Andreani, L. and Korup, O. (2021) How robust are  
709 landslide susceptibility estimates? Landslides **18**, 681–695.

710 Papathoma-Köhle, M., Zischg, A., Fuchs, S., Glade, T. and Keiler, M. (2015) Loss estimation for  
711 landslides in mountain areas—An integrated toolbox for vulnerability assessment and damage  
712 documentation. Environmental Modelling & Software **63**, 156–169.

713 Pascale, S., Sdao, F. and Sole, A. (2010) A model for assessing the systemic vulnerability in landslide  
714 prone areas. Natural Hazards and Earth System Sciences **10**(7), 1575–1590.

715 Peduto, D., Ferlisi, S., Nicodemo, G., Reale, D., Pisciotta, G. and Gullà, G. (2017) Empirical fragility  
716 and vulnerability curves for buildings exposed to slow-moving landslides at medium and large scales.  
717 Landslides **14**, 1993–2007.

718 Pellicani, R., Van Westen, C. J. and Spilotro, G. (2014) Assessing landslide exposure in areas with limited  
719 landslide information. Landslides **11**, 463–480.

720 Petley, D. (2012) Global patterns of loss of life from landslides. Geology **40**(10), 927–930.

721 Petschko, H., Brenning, A., Bell, R., Goetz, J. and Glade, T. (2014) Assessing the quality of landslide  
722 susceptibility maps—case study Lower Austria. Natural Hazards and Earth System Sciences **14**(1),  
723 95–118.

724 Quan Luna, B., Blahut, J., Van Westen, C., Sterlacchini, S., van Asch, T. W. and Akbas, S. (2011) The  
725 application of numerical debris flow modelling for the generation of physical vulnerability curves.  
726 Natural hazards and earth system sciences **11**(7), 2047–2060.

727 Reichenbach, P., Rossi, M., Malamud, B. D., Mihir, M. and Guzzetti, F. (2018) A review of statistically-  
728 based landslide susceptibility models. Earth-Science Reviews **180**, 60–91.

729 Remondo, J., Bonachea, J. and Cendrero, A. (2008) Quantitative landslide risk assessment and mapping  
730 on the basis of recent occurrences. Geomorphology **94**(3-4), 496–507.

731 Roberts, D. R., Bahn, V., Ciuti, S., Boyce, M. S., Elith, J., Guillera-Arroita, G., Hauenstein, S., Lahoz-  
732 Monfort, J. J., Schröder, B., Thuiller, W., et al. (2017) Cross-validation strategies for data with  
733 temporal, spatial, hierarchical, or phylogenetic structure. Ecography **40**(8), 913–929.

734 Rossi, M., Guzzetti, F., Reichenbach, P., Mondini, A. C. and Peruccacci, S. (2010) Optimal landslide  
735 susceptibility zonation based on multiple forecasts. Geomorphology **114**(3), 129–142.

736 Rossi, M., Guzzetti, F., Salvati, P., Donnini, M., Napolitano, E. and Bianchi, C. (2019) A predictive  
737 model of societal landslide risk in Italy. Earth-Science Reviews **196**, 102849.

738 Rossi, M., Peruccacci, S., Brunetti, M., Marchesini, I., Luciani, S., Ardizzone, F., Balducci, V., Bianchi,

739 C., Cardinali, M., Fiorucci, F., et al. (2012) SANF: National warning system for rainfall-induced  
740 landslides in Italy. Landslides and engineered slopes: protecting society through improved  
741 understanding **2**, 1895–1899.

742 Sakamoto, Y., Ishiguro, M., Kitagawa, G., 1986. Akaike information criterion statistics. Dordrecht, The  
743 Netherlands: D. Reidel 81, 26853.

744 Samia, J., Temme, A. J., Bregt, A., Wallinga, J., Guzzetti, F., Ardizzone, F. and Rossi, M. (2017) Do  
745 Landslides Follow Landslides? Insights in Path Dependency from a Multi-Temporal Landslide  
746 Inventory. Landslides **14**, 547–558.

747 Schlögel, R., Marchesini, I., Alvioli, M., Reichenbach, P., Rossi, M. and Malet, J.-P. (2018) Optimizing  
748 landslide susceptibility zonation: Effects of DEM spatial resolution and slope unit delineation on logistic  
749 regression models. Geomorphology **301**, 10–20.

750 Segoni, S., Piciullo, L. and Gariano, S. L. (2018) A review of the recent literature on rainfall thresholds for  
751 landslide occurrence. Landslides **15**(8), 1483–1501.

752 Seijmonsbergen, A. et al. (2013) The modern geomorphological map. In: Methods in geomorphology, Elsevier,  
753 Amsterdam, pp.35-52.

754 Steger, S., Brenning, A., Bell, R. and Glade, T. (2016) The propagation of inventory-based positional  
755 errors into statistical landslide susceptibility models. Natural Hazards and Earth System Sciences **16**(12),  
756 2729–2745.

757 Steger, S., Moreno, M., Crespi, A., Zellner, P. J., Gariano, S. L., Brunetti, M. T., Melillo, M., Peruccacci,  
758 S., Marra, F., Kohrs, R. et al. (2022) Deciphering seasonal effects of triggering and preparatory  
759 precipitation for improved shallow landslide prediction using generalized additive mixed models. Natural  
760 Hazards and Earth System Sciences Discussions pp. 1–38.

761

762 Steger, S., Moreno, M., Crespi, A., Zellner, P. J., Gariano, S. L., Brunetti, M. T., Melillo, M., Peruccacci,  
763 S., Marra, F., Kohrs, R. et al. (2023) Deciphering seasonal effects of triggering and preparatory  
764 precipitation for improved shallow landslide prediction using generalized additive mixed models. Natural  
765 Hazards and Earth System Sciences **23**(4), 1483–1506.

766 Taylor, K. E., Stouffer, R. J. and Meehl, G. A. (2012) An overview of CMIP5 and the experiment  
767 design. Bulletin of the American Meteorological Society **93**(4), 485–498.

768 Thrasher, B., Maurer, E. P., McKellar, C., and Duffy, P. B. (2012) Technical Note: Bias correcting  
769 climate model simulated daily temperature extremes with quantile mapping. Hydrology and Earth  
770 System Sciences **16**(9), 3309–3314.

771 Titti, G., van Westen, C., Borgatti, L., Pasuto, A. and Lombardo, L. (2021) When enough is really



772 enough? on the minimum number of landslides to build reliable susceptibility models. Geosciences  
773 **11**(11), 469.

774 Tyagi, A., Tiwari, R. K. and James, N. (2022) A review on spatial, temporal and magnitude prediction of  
775 landslide hazard. Journal of Asian Earth Sciences: **X** p. 100099.

776 Uzielli, M., Catani, F., Tofani, V. and Casagli, N. (2015) Risk analysis for the Ancona landslide—  
777 II: estimation of risk to buildings. Landslides **12**, 83–100.

778 Van Den Eeckhaut, M., Reichenbach, P., Guzzetti, F., Rossi, M. and Poesen, J. (2009) Combined  
779 landslide inventory and susceptibility assessment based on different mapping units: an example from  
780 the Flemish Ardennes, Belgium. Natural Hazards and Earth System Sciences **9**(2), 507–521.

781 Van Westen, C., Van Asch, T. W. and Soeters, R. (2006) Landslide hazard and risk zonation—  
782 why is it still so difficult? Bulletin of Engineering Geology and the Environment **65**(2), 167–184.

783 Wadoux, A. M.-C., Heuvelink, G. B., De Bruin, S. and Brus, D. J. (2021) Spatial cross-validation is  
784 not the right way to evaluate map accuracy. Ecological Modelling **457**, 109692.

785 Wang, L., Yin, Y., Zhang, Z., Huang, B., Wei, Y., Zhao, P., and Hu, M. (2019) Stability analysis of  
786 the Xinlu Village landslide (Chongqing, China) and the influence of rainfall. Landslides **16**, 1993–  
787 2004.

788 Wang, N., Cheng, W., Marconcini, M., Bachofer, F., Liu, C., Xiong, J. and Lombardo, L. (2022a)  
789 Space-time susceptibility modeling of hydro-morphological processes at the Chinese national scale.  
790 Engineering geology **301**, 106586.

791 Wang, Z., Goetz, J. and Brenning, A. (2022b) Transfer learning for landslide susceptibility modeling  
792 using domain adaptation and case-based reasoning. Geoscientific Model Development **15**(23), 8765–  
793 8784.

794 Wood, S. and Wood, M.S., 2015. Package ‘mgcv’. R package version, 1(29), p.729.

795 Yilmaz, I. (2010) The effect of the sampling strategies on the landslide susceptibility mapping by conditional  
796 probability and artificial neural networks. Environmental Earth Sciences **60**, 505–519.

797 Zhang, W., He, Y., Wang, L., Liu, S. and Meng, X. (2023) Landslide Susceptibility mapping using random  
798 forest and extreme gradient boosting: A case study of Fengjie, Chongqing. Geological Journal.

799 Zhao, L., Zuo, S., Deng, D., Han, Z. and Zhao, B. (2018) Development mechanism for the landslide at  
800 Xinlu Village, Chongqing, China. Landslides **15**, 2075–2081.